Thorax oncology : a hierarchical segmentation framework incorporating bi-modality PET/CT images specificities and shape constraints to segment tumors and organs at risk

Oncologie thoracique : une approche hiérarchique intégrant les spécificités des images TEP/TDM et des contraintes de formes pour segmenter des tumeurs et organes à risque

---

Julien Wojak
Elsa D. Angelini
Isabelle Bloch

2010D016

Juillet 2010

Département Traitement du Signal et des Images
Groupe TII : Traitement et Interprétation des Images

Thorax oncology: a hierarchical segmentation framework incorporating bi-modality PET/CT images specificities and shape constraints to segment tumors and organs at risk

Oncologie thoracique : une approche hiérarchique intégrant les spécificités des images TEP/TDM et des contraintes de formes pour segmenter des tumeurs et organes à risque

Julien Wojak[1], Elsa D. Angelini[1], Isabelle Bloch[1]

[1] Institut Télécom, Télécom ParisTech, CNRS LTCI, Paris, France

July 8, 2010

Abstract

In thoracic oncology, PET and CT imaging are more and more used conjointly, in particular thanks to the development of combined scanners. Radiotherapy planning is usually based on CT images, and requires the segmentation of pathologies, such as tumors and infected lymph nodes, as well as of organs at risk, in order to carefully design the radiation region. In this work, we propose a complete framework to segment thoracic organs using information provided by the dual modality PET/CT images, and a priori knowledge about organ shapes. Segmentations are performed hierarchically in a sequential scheme using a robust variational method. To specifically segment tumors or lymph nodes, the bi-modality imaging PET/CT is exploited, and the PET information is used to constrain the CT segmentation. To segment organs at risk, shape constraints, based on translation and scale invariant Legendre moments, are used. In both cases, quantitative results show the agreement with manual segmentation, and the interest of the proposed approaches.

Résumé

En imagerie pour l'oncologie du thorax, les images TDM (tomodensitométriques) et les images TEP (tomographie à émission de positons) sont de plus en plus fréquemment utilisées conjointement grâce au développement des machines combinées. De plus, les plans de traitement pour la

*Acknowledgments: This work was partially funded by the Medicen Pôle de Compétitivité within the Miniara project.

radiothérapie n'utilisent habituellement que des images TDM et nécessitent, pour définir une zone d'irradiation optimale, une segmentation des pathologies (comme des tumeurs ou des lymphomes) et des organes risques. Dans ce rapport, nous proposons une méthodologie pour segmenter les organes et les pathologies du thorax en utilisant la bimodalité TEP/TDM et des informations a priori sur la forme de certains organes. Les segmentations sont réalisées séquentiellement en suivant une description hiérarchique de l'anatomie du thorax (sous forme d'arbre d'inclusion) reposant sur des propriétés des distributions d'intensité des images TDM. Des méthodes variationnelles robustes sont mise en œuvre à chacune des segmentations. Plus spécifiquement, les segmentations des tumeurs et des lymphomes sont réalisées à partir des couples d'images TEP/TDM, en contraignant la segmentation sur l'image TDM par des informations provenant de l'image TEP. Les segmentations des organes à risque sont contraintes par des informations de forme, décrites par des moments de Legendre invariants par translation et changement d'échelle. Dans chacun des cas, des résultats quantitatifs de comparaison avec des segmentations manuelles réalisées par des experts montrent les bonnes performances des approches proposées.

1 Introduction

Lung cancers and/or thoracic lymph node oncological infections rely on imaging for diagnosis and radiotherapy planning techniques. Several imaging modalities may be involved. In the particular case of thoracic oncology, the two main modalities are F18-PET and CT imaging. The PET modality provides functional information and is useful to detect and/or quantify tumors activity. CT images provide more precise anatomical information. As argued in [1] the reference image modality for those tasks is the CT scan. The need for segmentation of infected lymph nodes or lung tumors is important in particular for quantification and follow up purposes. However manual segmentations performed by medical experts are tedious and subject to intra and inter-pratician variability [2, 3]. In the context of radiotherapy planning, not only pathological structures must be segmented but also organs at risks. Organs at risk are anatomical structures which show a relatively high sensitivity to radiations with subsequent functional impairment at therapeutic doses. For example the heart constitutes an organ at risk. Its segmentation then allows designing carefully the radiation region.

In this work we propose a complete framework to segment thoracic organs using information provided by the dual modality PET/CT images and a priori knowledge about organ shapes. Segmentations are performed hierarchically in a sequential framework using a robust variational method. To specifically segment tumors or lymph nodes, the bi-modality imaging PET/CT is used. To segment organs at risk, shape constraints, based on translation and scale invariant Legendre moments, are used.

Using a hierarchical and sequential scheme to segment anatomical objects is a common methodology. In [4, 5] the interest of hierarchical descriptions of the image content to guide a full segmentation process is shown. More specifically, in [5] a complete methodology to hierarchically and sequentially create regions of interest is proposed and examples of sequential abdomen organs segmentations are shown.

In whole body CT imaging a sequential framework to successively segment the lungs, liver and kidneys is used in [6]: first the body and lungs are segmented and then using knowledge about the lungs, the liver is segmented to finally lead to the segmentation of the kidneys. However, even in CT scan images, where intensities are quite stable, a hierarchical model alone is not sufficient to segment pathologies such as tumors or infected lymph nodes and low contrasted organs at risk such

as the heart. To overcome this difficulty we propose to incorporate additional source of information and knowledge, provided by the PET image for tumor and lymph nodes, and by shape constraints for the non contrasted organs at risk.
When tumors are present in the lungs, they show similar intensity values as the pulmonary vessels. A hierarchical segmentation framework, only based on image intensity, will therefore fail to correctly separate them from pulmonary vessels. However nowadays combined PET/CT scanners are routinely used. In oncological applications, PET images provide functional information about the metabolism activity (with high fixation of the FDG tracer observed in tumoral regions).We propose to jointly use these two modalities to segment tumors. Among the few papers dealing with this problem, we can cite [7] where a multimodal image segmentation based on the active contour of Chan and Vese [8] is formulated for multi-channel images. Promising results were obtained but the method was very sensitive to the initialization setup. In [9] after detecting tumors as local maxima in the PET image, segmentation was performed with a joint likelihood ratio test. In [10] a classification framework based on MAP-MRF models was applied on PET-CT vectorial images. In all these previous works, perfect registration of the two modalities was assumed, which is not always a realistic hypothesis even for combo scanners and especially in thoracic images where breathing movements are difficult to control.
Like tumors, organs at risk are often difficult to segment with only the CT scan gray level intensity. For example, the heart and the liver have a quite similar intensity and there is not always reliable gradient information between them. To overcome this difficulty, a common idea is to add shape information in the segmentation framework. Several methods have been proposed to constraint a segmentation process with shape information. In the class of variational segmentation methods, a shape constraint term is often added in the functional. In [11], shape constraint is used to segment image on a video. A distance between a reference shape (provided by the previous frame segmentation) and the shape of the segmentation (in the current frame) is used to add a term in an active contour formulation. Instead of using a single shape of reference, in [12] Leventon used a training set of shapes. As in [13] a PCA analysis is done on the training set to highlight the principal variations of a shape. However, the PCA is not done directly on a parametric representation of the shape but on the signed distance functions of the contours of the shape. Then a term taking into account the shape information is added in the framework of geodesic active contours. A similar approach was developed in [14] using only the first few deformation modes. Similar ideas were developed in [15, 16, 17] and a review of shape constraints for level sets segmentation methods can be found in [18]. For the foreseen thoracic radiotherapy application, we have to achieve a compromise between discriminant shape characterization and the flexibility of the shape representation to cope with inter-patient variability (patient positioning, heart size ...). In this context it might be not relevant to directly compute a difference between a reference shape and the current shape segmentation. We propose rather to control an indirect match by comparing the deforming shape with a generic shape model representation that does allow natural anatomic variability. The shape representation must be invariant to translation and scale . Such characteristics can be provided by well-chosen shape moments. For example in [19], Tchebichev moments were used to constrain a region growing algorithm, and Foulonneau et al. [20], and then Lecellier et al. [21], used Legendre moments as shape descriptors within an active contour segmentation framework. Our approach follows a scheme similar to [20], with differences outlined in Section 6.3.
In the following of this paper, we first describe the CT imaging modality, its specifities and its useful features to perform segmentation of thoracic regions for radiotherapy planning (Section 2). In Section 3, we describe a robust variational segmentation method. Then, in Section 4 we describe

a hierarchical framework to perform segmentation. Finally we show how to incorporate PET information to segment malignant tissues on the one hand (Section 5) and, on the other hand, how to incorporate shape constraints to segment organs at risk (Section 6).

2 Thoracic CT-scan images: description and properties

CT images are calibrated and the value of each voxel is expressed in Hounsfield Units (HU) (air is -1000 HU, water is 0 HU and compact bones are +1000 HU). Figure 1 shows the typical intensity distribution in a CT image in Hounsfield units as described in [22].

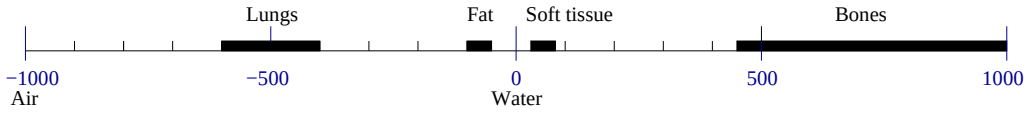

Figure 1: CT intensity distribution in Hounsfield Units (HU) [22].

From those absolute intensities, we can derive a hierarchical description of the thorax as a tree representing a hierarchical inclusion of thoracic structures. This tree is represented in Figure 2. Each node of the tree represents a thoracic meaningful anatomical structure included in its parent node. The root of the tree represents the whole CT image. Its two children are the whole body and the background (bed, air, and other elements as blanket). As the background does not contain any structure of interest, it is a terminal node. The whole body could also be split into two meaningful anatomical structures: airways and other tissues. Airways are then decomposed in trachea and lungs and then lungs into parenchyma and lung vessels. At the same time, other tissues are decomposed into bones and soft tissues and then soft tissues are decomposed into dark (muscles) and bright soft tissues (fat).
We observe in the CT image intensity histogram, that each pair of nodes decomposes the distribution intensity into two non overlapping distributions. Figure 4 illustrates this separation between the whole body and airways and between lungs and trachea. The proposed tree construction is based on such histogram decomposition. Figure 4 illustrates the separation between modes, at the fourth level of the anatomical decomposition tree, for the histogram of the lungs and trachea.
Those a priori intensity distributions separations in a hierarchical tree will be used (in Section 4) to construct a data-fidelity term in the variational segmentation method described in Section 3.

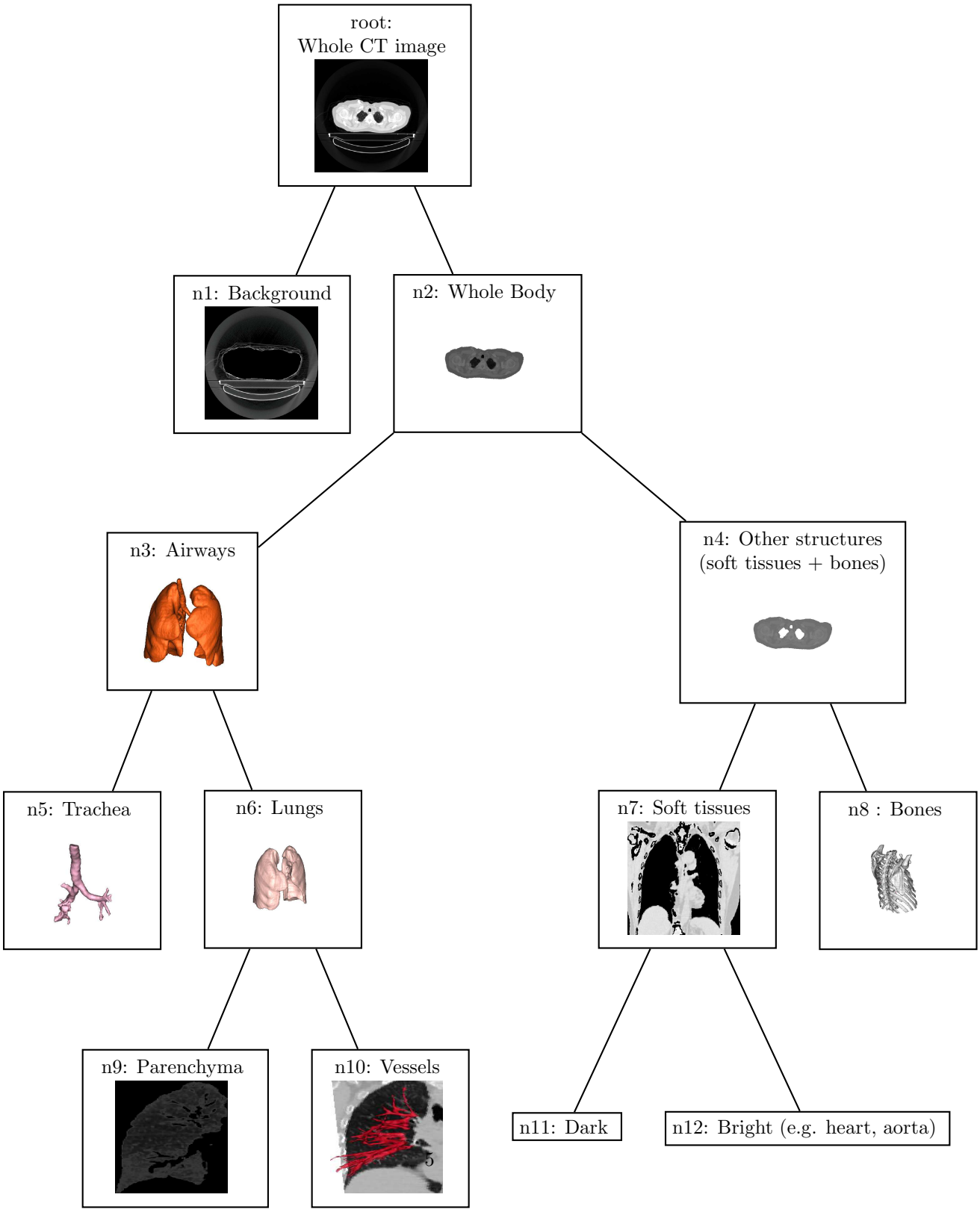

Figure 2: CT-based hierarchical anatomical description of thoracic organs

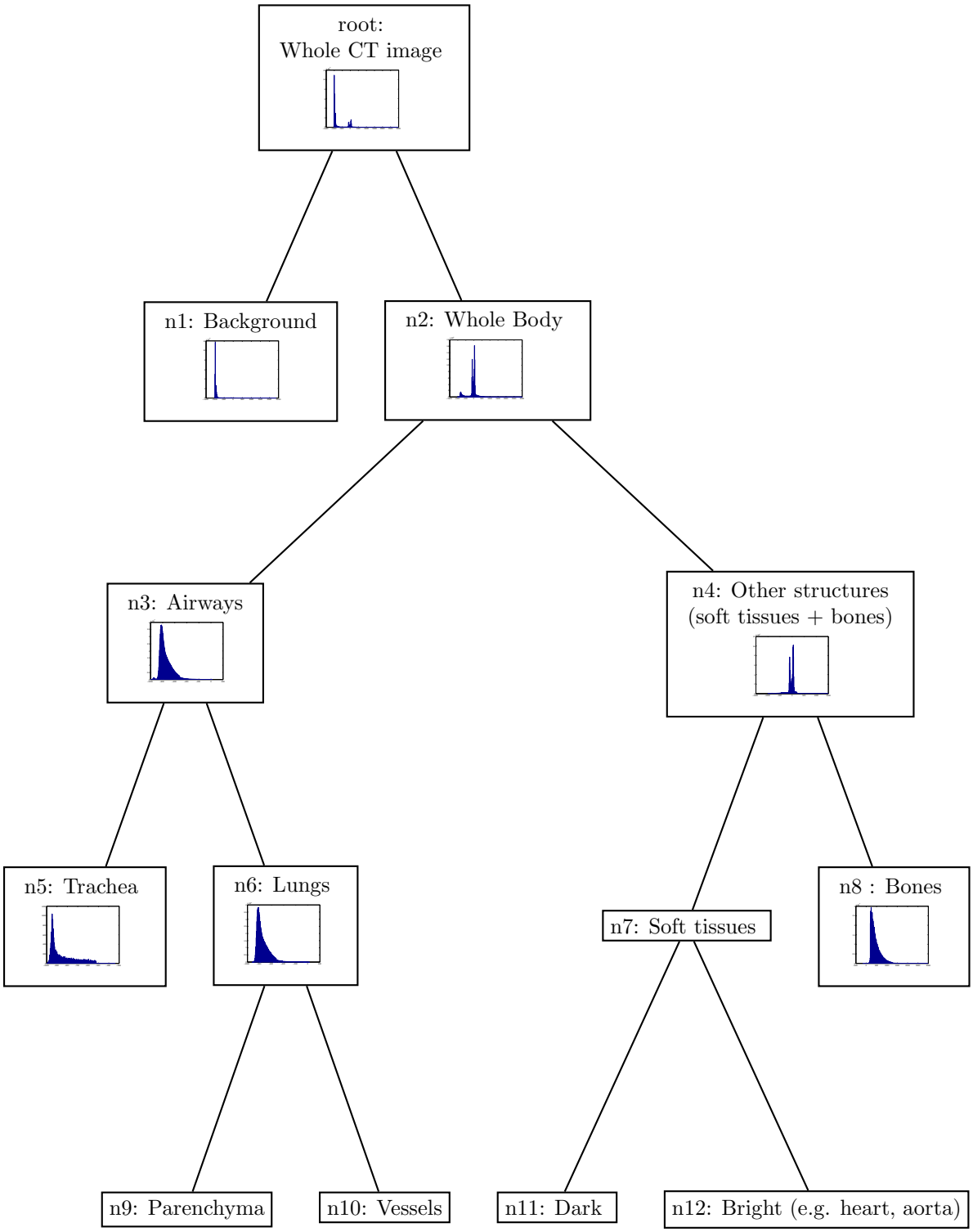

Figure 3: Analysis of the intensity distribution in a typical calibrated CT scan image. In this binary tree each node represents a sub-domain of the image included in its parent.

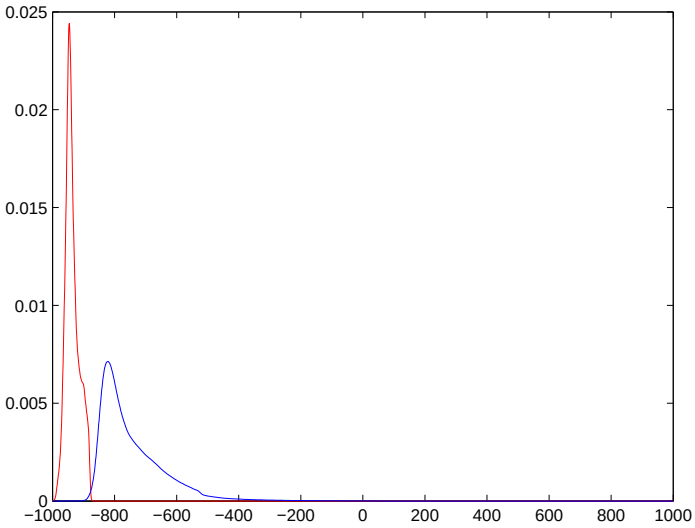

Figure 4: Probability density function estimations of the intensity of the lungs (blue) and the trachea (red) showing two separated peaks.

3 Variational segmentation based on gray level intensity

Variational image segmentation methods consist in finding contours or regions in a given image I by minimizing an appropriate energy functional. For example in the piecewise-constant Mumford-Shah image segmentation model from Chan-Vese [8], the functional is expressed as:

$$E_{CV}(C, c_1, ..., c_l) = \text{length}(C) + \lambda \sum_{l=1}^{L} \int_{\Omega_l} (I(x) - c_l)^2 \text{d}\Omega \tag{1}$$

where $\Omega_l,\ l = 1..L$, is a partition of the image I domain Ω ($\Omega \subset \mathbb{R}^n$, $n = 2$ or 3) in L regions Ω_l, C being the set of curves that delimit the regions, and c_l are constant values characterizing the average value within the regions. The parameter λ controls the trade-off between data fidelity and regularity terms.

The solution is a partition of the image in L phases (i.e. regions), each phase having a constant intensity (the optimal c_l value) and the length of the region contours being constrained to avoid oscillations and to provide a regularized solution.

A common approach to minimize Equation (1) with two phases (foreground and background) is detailed in [8], embedding the contour formulation into a level-set framework (eq. 2) and computing the Euler-Lagrange equations for the optimization of the energy parameters via gradient descent.

$$\min_{\phi,c_1,c_2} E(\phi, c_1, c_2) = \min_{\phi,c_1,c_2} \left[\int_\Omega |\nabla H(\phi)| d\Omega + \lambda \int_\Omega H(\phi)(I - c_1)^2 d\Omega + \lambda \int_\Omega (1 - H(\phi))(I - c_2)^2 d\Omega \right] \tag{2}$$

where ϕ is the level set function, H a characteristic -or Heavyside- function and λ a parameter that controls the trade-off between the regularity and the data fidelity.

The major drawback of this method is the existence of local minima of the functional, making the quality of image segmentation sensitive to the initialization.

3.1 Fuzzy segmentation model

In [23, 24, 25] an alternative segmentation framework is proposed, directly looking for optimal Ω_i as an optimal function measuring the membership to each region (and no longer using characteristic functions). Let $u \in BV_{[0,1]}(\Omega)$ (the space of functions of bounded variations defined on Ω and taking their values in $[0,1]$) be a fuzzy membership function suited for the segmentation problem, e.g. $u \approx 0$ in the background and $u \approx 1$ in the foreground. The following functional is proposed (using similar notations as in Equation (1)) :

$$\begin{aligned}\min_{u\in BV_{[0,1]}(\Omega),c1,c2} E_{TV_g}(u,c1,c2) = \min_{u\in BV_{[0,1]}(\Omega),c_1,c_2} \Big[\int_\Omega g|\nabla u|\mathrm{d}\Omega \\ + \lambda\int_\Omega u(I-c_1)^2\mathrm{d}\Omega + \lambda\int_\Omega (1-u)(I-c_2)^2\mathrm{d}\Omega\Big]\end{aligned} \tag{3}$$

The regularity of the segmented regions is controlled by constraining the total variation (TV) semi-norm of the membership function. As in [24], the TV semi-norm is weighted by a contour map g (for example $g = \frac{1}{1+|\nabla I|}$) to allow less regularization where contours are clearly visible.

This image segmentation formulation has two very important properties: (i) For fixed c_i, the problem (3) is convex in u, and therefore has a global minimum. There exist very efficient algorithms to minimize (3) with respect to u. (ii) The global minimizer of u is guaranteed to be close to a characteristic function. A contour can therefore be simply obtained by thresholding u at any level α with $0 < \alpha < 1$. Proofs of these properties are detailed in [23, 24, 26]. These properties have guided our choice of this type of method.

3.2 Efficient minimization

To solve Equation (3), an alternate minimization is iterated, first fixing u and optimizing c_i and then fixing c_i and optimizing u, until convergence. Minimization with respect to c_i is performed with these explicit formulations:

$$c_1 = \frac{\int_\Omega uI\mathrm{d}\Omega}{\int_\Omega u\mathrm{d}\Omega} \quad \text{and} \quad c_2 = \frac{\int_\Omega (1-u)I\mathrm{d}\Omega}{\int_\Omega (1-u)\mathrm{d}\Omega} \tag{4}$$

When the c_i are fixed, the minimizer u^* of Equation (3) is the same as the minimizer of:

$$\min_{u\in BV_{[0,1]}(\Omega)} E_{TV_g}(u) = \min_{u\in BV_{[0,1]}(\Omega)} \Big[\int_\Omega g|\nabla u|\mathrm{d}\Omega + \lambda\int_\Omega ur\mathrm{d}\Omega\Big] \tag{5}$$

with $r = (I-c_1)^2 - (I-c_2)^2$.
As in [24], other region competition functions r could be used, such as statistical comparison of estimated region probability densities functions.
To minimize Equation (5) with respect to u under the constraint $u \in BV_{[0,1]}(\Omega)$, the following equivalent unconstrained problem can be written (the proof is given in [26]):

$$\min_u E_{TV_g}(u) = \min_u \Big[\int_\Omega g|\nabla u|\mathrm{d}\Omega + \int_\Omega \lambda ur + \beta\nu(u)\mathrm{d}\Omega\Big] \tag{6}$$

where the penalty term ν is given by $\nu(t) = \max(0, |2t-1|-1)$ and $\beta > \frac{1}{2}|r|_\infty$. The problem (6) could be solved with Euler-Lagrange equations and gradient descent. However this method is slow and since the terms $|\nabla u|$ and $\nu(t)$ are not differentiable, they must be regularized, which implies a slower gradient descent. To avoid these two problems, as in [24], it is preferable to use the fast duality projection algorithm proposed in [27]. This algorithm is based on a weak approximation of Equation (6) by introducing an auxiliary variable v (and a parameter θ):

$$\min E_{TV_{g2}}(u,v) = \min \Big[\int_\Omega g(x)|\nabla u| \mathrm{d}\Omega + \frac{1}{2\theta}\int_\Omega |u-v|^2 \mathrm{d}\Omega + \int_\Omega \lambda v r + \beta\nu(v)\mathrm{d}\Omega \Big] \tag{7}$$

This approximation is suitable if the minimizers u^* and v^* are almost identical w.r.t. the L^2 norm. To ensure this condition, θ must be set to a small value. Equation (7) is minimized with an alternate scheme described in Algorithm 1.

Algorithm 1 Minimization

Require: $I, u, \theta, \tau, g, \lambda$
  repeat
    compute c_1 and c_2 by (4)
    $r := \lambda[(I-c_1)^2 - (I-c_2)^2]$
    $v := \max(\min(u-\theta r, 1), 0)$
    $p^0 := 0$
    repeat
      $p^{n+1} := \frac{p^n + \frac{1}{8}\nabla(div(p^n) - \frac{v}{\theta})}{1 + \frac{1}{8}|\nabla(div(p^n) - \frac{v}{\theta})|}$
    until $p^{n+1} \approx p^n$
    $u := v - div(p)$
  until convergence

Thanks to this formulation, since the functional 3 is convex, we have a robust method to segment an image into two constant piecewise phases. Moreover, thanks to Algorithm 1, the minimization process is fast.

3.3 Region competition term

In some cases, assuming constant intensity foreground (c_1) and background (c_2) is not relevant and it is more appropriate to fit foreground and background appearances with known or estimated probability density functions.

Expression of homogeneity term with known foreground and background pdf If the pdf of the foreground (i.e. a structure of interest s) and the background are known, we could use a formulation as in [28, 18, 29]. Assuming that the pdf of s in the image ($p_s(I(\mathbf{x}))$) depends on parameters θ_s and the background pdf ($p_b(I(\mathbf{x}))$) depends on parameters θ_b, the data fidelity term can be expressed as $r(\mathbf{x}) = (\ln(p_s(I(\mathbf{x})|\theta_s)) - \ln(p_b(I(\mathbf{x})|\theta_f)))$.

Estimation of foreground and background pdf Kernel density estimation (also called Parzen estimation) could be used in the previous formulation. It is a non parametric technique to estimate

the probability density function of a random variable. Let us assume that an image is composed by a structure of interest s and a background b and that the image intensity in s, resp. in b, is the realization of a random variable I_s, resp. I_b, described by its probability density function $P(I_s)$, resp. $P(I_b)$. The kernel density estimation consists in evaluating $P(I_s)$ and $P(I_b)$ from empiric distributions such as gray level histograms. It is expressed as

$$P(I_s = a) = \frac{1}{nh_s} \sum_{i=1}^{n} K\left(\frac{a - d_i^s}{h_s}\right) \quad \text{and} \quad P(I_b = a) = \frac{1}{mh_b} \sum_{i=1}^{m} K\left(\frac{a - d_i^b}{h_b}\right) \tag{8}$$

where the dynamic of s is quantified in a vector d^s of size n an the dynamic of b is quantified in a vector d^b of size m.
The parameters h_s and h_b define the bandwidth of K, and K is a Gaussian kernel ($K(t) = \frac{1}{\sqrt{2\pi}} \exp -(\frac{1}{2}t^2)$). Figure 5 illustrates the estimation of the body intensity with a Gaussian kernel using three differents bandwidths (5,25,75).

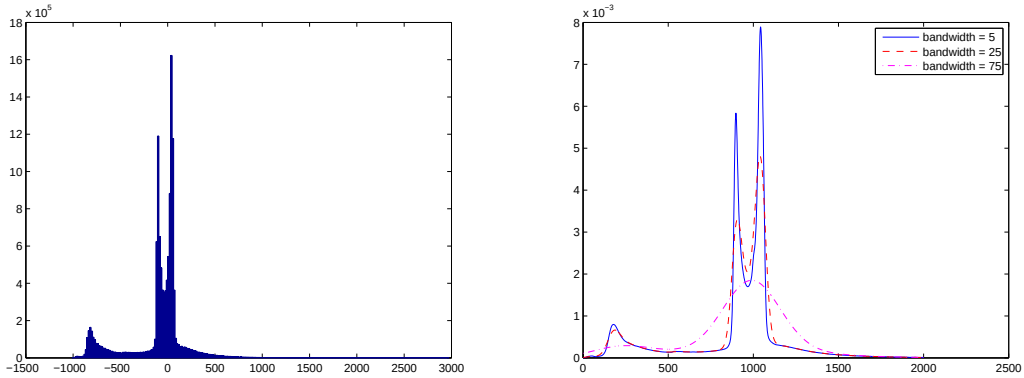

Figure 5: Parzen probability density estimation of the intensity distribution of the body. Bandwith are equal to 5 (plain line), 25 (dashed line), 75 (dotdashed).

As shown in Section 2, the CT based intensity histograms in the different anatomical structures are quite stable due to the calibrated nature of this imaging modality. We can use those histograms, to construct, with Parzen density estimations, the density probability functions of the intensities of each anatomical structure. In the following section, we show how to define those probability density functions and use them to perform segmentations sequentially according to the tree description.

4 Hierarchical segmentation framework

In [30] an unsupervised multiphase segmentation using a recursive approach is presented. It recursively applies the two phase constant approximation algorithm in each of the two newly created sub-regions until the segmentation does not identify any further separation. In our context, as presented in Section 2, strong knowledge about objects to be segmented in the scene could be built on. It allows us to use a supervised hierarchical and sequential approach.

Estimation of the pdf of the main structures in CT scan

Following the hierarchical tree construction method, a sequential process is proposed. It consists in segmenting the two phases corresponding to the two children of a tree node, with the previous region competition method. We begin by the root of the tree and separate the whole body (node n2) from the background (node n1). As the background is a terminal node, we stop the process for this branch. Then we mask the whole body to separate airways (node n3) from other tissues (node n4) corresponding to soft tissues and bones. From those two new nodes, we reiterate the segmentation process. It stops when each terminal node is segmented.

To obtain a satisfying segmentation at each level of the hierarchy, the region competition term is built in order to have a strong match between the expected intensity distribution of each structure (estimated from a typical CT image), and the intensity distribution of the currently segmented structures.

Construction of the region competition term Let I be the gray level image and $I(\mathbf{x})$ its value at point $\mathbf{x}$. Depending on the level in the hierarchical tree, s could represent the body, lungs, trachea, etc. Finally let us impose the convention that for each node in the hierarchical tree, the left child has the darkest intensity mean value, and the right child has the brightest intensity mean value. In a generic way, the background denotes the left child and the structure s denotes the right child. As in [28] we want to maximize the likelihood of the structure s and its background b:

$$L(I|\{s,b\}) = \prod_{\mathbf{x}\in s} P(I_s = I(\mathbf{x})) \prod_{\mathbf{x}\in b} P(I_b = I(\mathbf{x})) \tag{9}$$

Maximizing $L(I|\{s,b\})$ is equivalent to minimize $-\log P(I|\{s,b\})$.

Finally, the whole objective function is then rewritten as:

$$\min_u E = \min_u \left[\int_\Omega |\nabla u| + \int_\Omega u \log(P(I_s = I(\mathbf{x}))) + (1-u)\log(P(I_b = I(\mathbf{x})))d\mathbf{x} \right] \tag{10}$$

Results of the minimization are shown for the to first levels of the tree construction in Figures 6 and 7.

Example of the first step: the separation of the body and other structures in the image (bed) is shown in Figure 6.

Second step: segmentation of lungs and trachea.

The domain Ω in reduced to the mask of the body area. The competition term is also built from the estimated probability density function of the body tissues without lungs.

The last level of the tree

At the last levels of the tree, structures have quite uniform intensity distributions. However they contain objects of interest. For example a tumor could be among lungs vessels, or interesting structures for radiotherapy planning still need to be segmented. We introduce another level of segmentation guidance such as functional imaging or knowledge about shape to cope with this issues.

Previous segmentations (in higher levels in the tree) are useful at this step to provide masks or regions of interest.

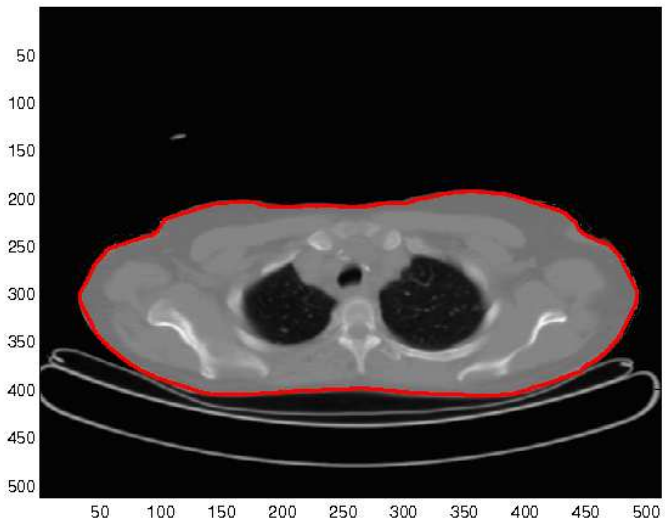

Figure 6: Whole body segmentation result.

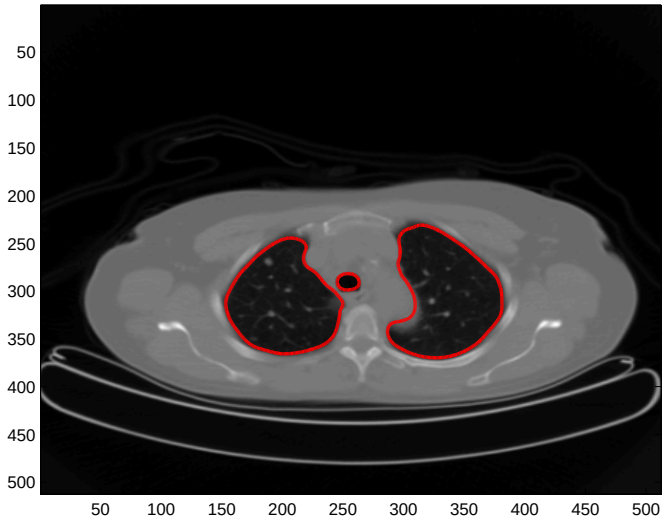

Figure 7: Airways segmentation result.

5 Tumors and infected lymph nodes segmentation

We now address the segmentation of pathologies using both CT an PET data.

5.1 Direct vectorial approach

For lung tumors it is often difficult to visually separate the tumor from the surrounding vessels or mediastinal tissues in CT image data. In this case, PET images can provide useful information to guide the segmentation on the CT images, highlighting only tumoral tissues.
Since the CT spatial resolution is much higher than the PET resolution, and in order to better preserve the 3D continuity of anatomical structures, we re-sampled the PET images via bi-linear interpolation to match the CT spatial resolution in terms of voxel sizes.
After re-sampling, a straightforward extension of the proposed segmentation framework can be tested, reformulating the energy functional to handle vectorial images, and leading to the following energy minimization problem:

$$\begin{aligned}&\min_{u\in BV_{[0,1]}(\Omega)} E_{TV_g}(u,\mathbf{c_1},\mathbf{c_2}) = \\ &\min_{u\in BV_{[0,1]}(\Omega)} \Big[\int_\Omega g|\nabla u|\mathrm{d}\Omega \\ &\qquad + \int_\Omega u||\Lambda(\mathbf{I}-\mathbf{c_1})||^2\mathrm{d}\Omega + \int_\Omega (1-u)||\Lambda(\mathbf{I}-\mathbf{c_2})||^2\mathrm{d}\Omega\Big]\end{aligned} \tag{11}$$

where $\mathbf{c_1} = (c_{1_1}, c_{1_2})^T$, $\mathbf{c_2} = (c_{2_1}, c_{2_2})^T$, $\mathbf{I} = (I_{CT}, I_{PET})^T$ are vectors in $\mathbb{R}^2$ and $\Lambda = \begin{pmatrix} \lambda_1 & 0 \\ 0 & \lambda_2 \end{pmatrix}$.
While this method is faster than the one described in [7], it still suffers from the sensitivity to the intrinsic mis-registration between the CT and the PET data. This is illustrated in Figure 8 (b) where the vectorial segmentation result for a lung tumor corresponds to the mean shape between the PET and the CT image information. Indeed, as shown in the following, minimizing 11 is equivalent to minimizing a functional composed by a weighted sum of a CT based term and a PET based term.

$$\min_{u\in BV_{[0,1]}(\Omega)} \Big[\int_\Omega g|\nabla u|\mathrm{d}\Omega + \int_\Omega u||\Lambda(\mathbf{I}-\mathbf{c_1})||^2\mathrm{d}\Omega + \int_\Omega (1-u)||\Lambda(\mathbf{I}-\mathbf{c_2})||^2\mathrm{d}\Omega\Big] \tag{12}$$

is equivalent to

$$\min_{u\in BV_{[0,1]}(\Omega)} \left[2\int_\Omega g|\nabla u|\mathrm{d}\Omega + 2\int_\Omega u\left\|\begin{pmatrix}\lambda_1 I_{CT}\\ \lambda_2 I_{PET}\end{pmatrix} - \begin{pmatrix}\lambda_1 c_{1_1}\\ \lambda_2 c_{1_2}\end{pmatrix}\right\|^2 + (1-u)\left\|\begin{pmatrix}\lambda_1 I_{CT}\\ \lambda_2 I_{PET}\end{pmatrix} - \begin{pmatrix}\lambda_1 c_{2_1}\\ \lambda_2 c_{2_2}\end{pmatrix}\right\|^2 \mathrm{d}\Omega\right] \tag{13}$$

i.e.,

$$\begin{aligned}&\min_{u\in BV_{[0,1]}(\Omega)} \Big[\int_\Omega g|\nabla u|\mathrm{d}\Omega + 2\int_\Omega u(\lambda_1 I_{CT} - \lambda_1 c_{1_1})^2 + (1-u)(\lambda_1 I_{CT} - \lambda_1 c_{2_1})^2\mathrm{d}\Omega \\ &\qquad + \int_\Omega g|\nabla u|\mathrm{d}\Omega + 2\int_\Omega u(\lambda_2 I_{PET} - \lambda_2 c_{1_2})^2 + (1-u)(\lambda_2 I_{PET} - \lambda_1 c_{2_2})^2\mathrm{d}\Omega\Big]\end{aligned} \tag{14}$$

that could be rewrite

$$\min_{u\in BV_{[0,1]}(\Omega)} \Bigg[\underbrace{\int_\Omega g|\nabla u|\mathrm{d}\Omega + 2\lambda_1^2 \int_\Omega u(I_{CT}-c_{1_1})^2 + (1-u)(I_{CT}-c_{2_1})^2\mathrm{d}\Omega}_{\text{CT based energy term}} + \underbrace{\int_\Omega g|\nabla u|\mathrm{d}\Omega + 2\lambda_2^2 \int_\Omega u(I_{PET}-c_{1_2})^2 + (1-u)(I_{PET}-c_{2_2})^2\mathrm{d}\Omega}_{\text{PET based energy term}} \Bigg] \tag{15}$$

Expressed in this form we can clearly see that writing a vectorial model is equivalent to minimize weighted sum between a CT based energy (with a weight equal to $2\lambda_1^2$) and a PET based energy (with a weight equal to $2\lambda_2^2$).

(a) (b) (c)

Figure 8: Averaging effect: (a) superimposed PET and CT images, (b) vectorial segmentation with fixed parameters, (c) segmentation with a spatially varying $\lambda(x)$.

To avoid this averaging effect, we propose an alternative approach in the following.

5.2 Locally adaptative use of PET information

PET information can be introduced in the segmentation method by favoring CT-based segmentation of tumors or lymph nodes in bright PET areas. We propose to implement this idea by using a spatially varying parameter λ.
We therefore reformulate the energy functional in Equation 3 as :

$$\begin{aligned}\min_{u\in BV_{[0,1]}(\Omega)} E_{TV_g}(u,c1,c2) = \min_{u\in BV_{[0,1]}(\Omega)} \Big[&\int_\Omega g|\nabla u|\mathrm{d}\Omega \\ &+ \int_\Omega \lambda(x)u(I-c_1)^2\mathrm{d}\Omega + \int_\Omega \lambda(x)(1-u)(I-c_2)^2\mathrm{d}\Omega \Big]\end{aligned} \tag{16}$$

The function $\lambda(x)$ must be designed so that it takes high values where we want the data fidelity term to be more important than the regularization term and the segmentation result to closely follow the CT information. Conversely when $\lambda(x)$ takes low values, the data fidelity term is less important than the regularization term and the oscillations of the object (e.g. the tumor) contours are minimized. The minimization process remains the same as the one described in Section 3 since

$\lambda(x)$ is not optimized but pre-defined.
For radiotherapy planning, clinicians use the PET data to segment the tumors or the lymph nodes. In [31] several lung tumors segmentation methods for PET images were discussed and evaluated. Most of the methods are based on simple image intensity thresholding. The most simple threshold values are set between 60% and 50% of the maximal uptake PET intensity. In [32] a threshold was computed from the mean PET intensity inside the whole body, based on a specific regression formula. In [33] a threshold at 60% of the maximal uptake intensity was criticized and a thresholding taking into account background PET intensity was proposed. The study in [31] revealed that thresholding at 60% leads to too small delineations of the tumors. We therefore considered that all voxels with intensity larger than 60% were inside the pathological structure (tumor or lymph node) to design our function $\lambda(x)$. Moreover, the PET intensity signal is intense inside the pathological structure and smoothly decreases around it, as illustrated in Figure 9 on intensity profiles accross a tumor and a lymph node. From these observations, we assessed that $\lambda(x)$ should be an increasing function of the PET intensity with the following properties:
– $\lambda(x)$ should take a constant high value M for x greater than 60% of the PET maximum intensity value;
– $\lambda(x)$ should take a low value m close to 0 for low PET values;
– $\lambda(x)$ should be an increasing function between m and M. The growth rate depends on the confidence we have in the intermediate PET values.
A sigmoid function is proposed to define $\lambda(x) = M\frac{1}{1+a\exp^{-bI(x)}} + m$ (where $I(x)$ represents the PET intensity centered in 0). The parameter a is set to 1, M which is the upper bound of the sigmoid is chosen such that the data fidelity term and the regularization term are comparable, m is the lower bound of the sigmoid and is set to 10^{-6} to have a vanishing data fidelity term when the PET signal is not intense, and b which controls the slope of the sigmoid transition is chosen in the empirical interval $[0.0055, 0.012]$ (with $b \in [0.0055, 0.012]$ the similarity index between a manual segmentation and an automated segmentation was always superior to 0.5 in our experiments).

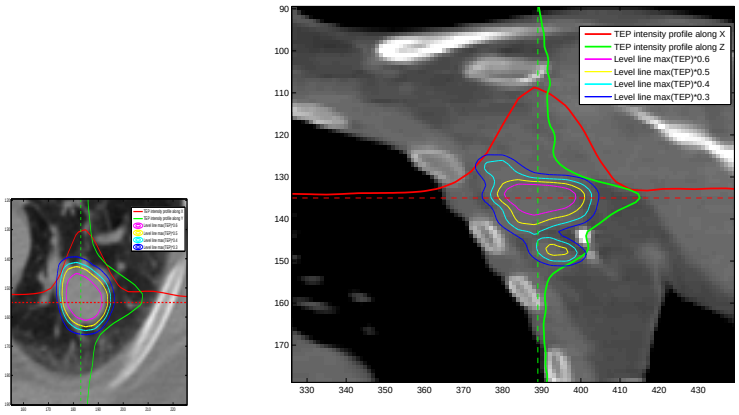

(a) (b)

Figure 9: PET intensity profiles overlaid on CT data for: (a) a lung tumor and (b) a lymph node. Level lines of PET intensity are superimposed for values between 0.6×max(PET) in red and 0.3×max(PET) in blue.

5.3 Clinical experiments and results

We evaluated the proposed segmentation framework on one case with lymphoma (presenting infected enlarged lymph nodes) and five cases with lung cancer (presenting tumors). CT-scans resolution is 1,17×1,17×1,60 mm^3 and PET resolution is 4×4×4 mm^3. The computation is done in a region of interest around the tumor. Some visual results are illustrated in Figures 8(c) and 11. To quantify the quality of the segmentation results, we compared them to manual segmentations of a clinical expert for the similarity, the sensitivity and the specificity indices. If we denote by E the set of voxels segmented by the expert,by A the set of voxel segmented by the automatic method and by $|E|$ and $|A|$ their cardinalities, the similarity index is given by $\frac{2|E \cap A|}{|E|+|A|}$, the sensitivity index by $\frac{|E \cap A|}{|E|}$ and the specificity index by $\frac{|E \cap A|}{|E|}$. They are reported in Table 1. All results were satisfactory for all cases, with higher accuracy on lung tumors.

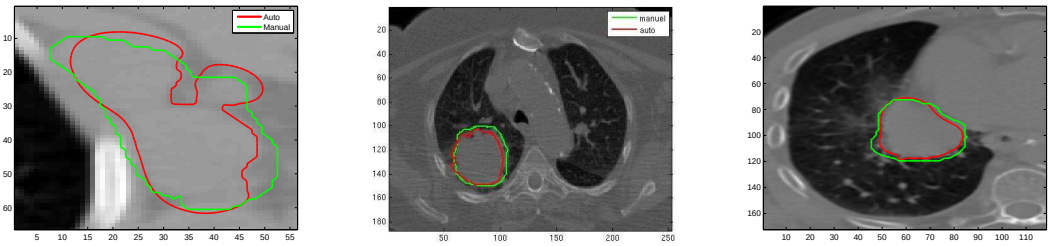

Figure 10: Segmentation results showing the manual segmentation (green) and the automatic segmentation (red) on three pathological cases: (left) thoracic lymph node, (middle-right) two large lung tumors in contact with the lung parenchyma.

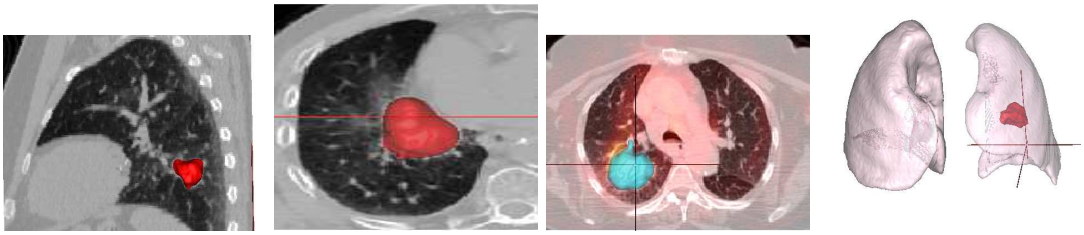

(a) (b) (c) (d)

Figure 11: 3D views of segmentation results. (a-b) A tumor superimposed on orthogonal slices of a CT scan, (c) the tumor superimposed on the fused PET-CT scan images, (d) 3D view of the tumor along with the lungs masks.

We also performed tests on images for which manual segmentations were not available. Overall qualitative results were very satisfactory in terms of robustness of the segmentation framework to low-contrast contours and mis-registration between the two imaging modalities. The variation between manual and automatic segmentations is in the range of inter-expert variability described

	Similarity index	Sensitivity	Specificity	Volume in cm^3 auto (manual)
tumor 1	0.85	0.76	0.96	80.07 (102.55)
tumor 2	0.79	0.68	0.96	11.97 (17.09)
tumor 3	0.81	0.78	0.89	14.12 (23.48)
tumor 4	0.90	0.86	0.95	48.90 (37.92)
tumor 5	0.82	0.79	0.84	3.48 (4.11)
lymph node	0.72	0.60	0.92	40.31 (78.41)

Table 1: Quantitative results: comparison of manual and automatic segmentations.

in [2]. However in difficult cases where the tumor is at the bottom of the lungs, close to the liver, some difficulties remain. Indeed PET intensity is also very high in the liver and does not allow us to discriminate the tumor in the lung. This problem could be solved by pre-segmenting the liver using for example the method described in [34].

6 Segmentation of organs at risk: introduction of shape constraints

In a radiotherapy treatment, organs at risk, such as the heart, must be preserved from radiation. The previous hierarchical model fails to segment organs at risk from other structures if they have similar intensity values. An example in Figure 12 illustrates the difficulty of separating the heart from adjacent structures such as the major blood vessels and the liver, on non-contrast CT data. In order to overcome such limitations, we propose to constrain the segmentation using shape information.

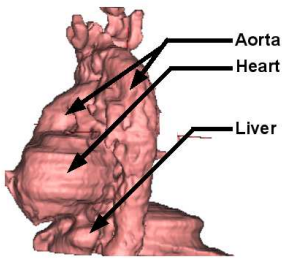

Figure 12: 3D visualization of CT Heart and iso-intense surrounding structures segmentation.

6.1 Legendre moments

In [35], Teague introduced the use of moments for image analysis. He proposed to use Legendre polynomials or Zernike polynomials as kernel functions. This choice was motivated by the orthogonality property of both types of polynomials, which guarantees the non-redundancy of the

description of an image or a shape. The existence of efficient methods to easily and fastly compute Legendre moments has guided our preference for these moments over Zernike ones. Legendre moments are more sensitive to noise than Zernike moments, but in our framework we manipulate descriptors only on clean binary masks or membership functions defined on $[0,1]$, in a framework of fuzzy region competition. Therefore this limitation is not a drawback for the proposed approach.

Legendre moments of an image $I : [-1,1]^3 \rightarrow \mathbb{R}$ are defined by its projection on a basis of polynomial functions. The moment of I of order $p+q+r$ is defined as:

$$\lambda_{pqr} = C_{pqr} \int_{[-1,1]^3} P_p(x) P_q(y) P_r(z) I(x,y,z) dx dy dz \tag{17}$$

where $C_{pqr} = \frac{(2p+1)(2q+1)(2r+1)}{8}$ and P_p,P_q,P_r are Legendre polynomials, defined by the following two order recursive relation:

$$P_{p+1}(x) = \frac{2p+1}{p+1} x P_p(x) - \frac{p}{p+1} P_{p-1}(x) \tag{18}$$

($p > 1$, $P_0(x) = 1$ and $P_1(x) = x$).
Legendre polynomials form an orthogonal basis, with:

$$\frac{2p+1}{2} \int_{-1}^{1} P_p(x) P_q(x) dx = \begin{cases} 0 & \text{if } p \neq q \\ 1 & \text{if } p = q \end{cases} \tag{19}$$

Working with a finite number of moments, an estimate $\hat{I}$ of I is given by:

$$\hat{I}(x,y,z) = \sum_{p=0}^{L} \sum_{q=0}^{p} \sum_{r=0}^{q} \lambda_{p-q,q-r,r} P_{p-q}(x) P_{q-r}(y) P_r(z) \tag{20}$$

where L is the maximum order for which Legendre moments are computed.

The computation can be performed with the fast and exact Hosny method [36]. First, the spatial image domain is embedded in the cube $U = [-1,1]^3$. Assuming that the image has $X \times Y \times Z$ voxels, the centers of voxels are then given by the coordinates (x_i, y_j, z_k) such that

$$\begin{array}{l} x_i = -1 + (i - 1/2)\Delta x \;\; i = 1 \cdots X \quad \text{and } \Delta x = \frac{2}{X} \\ y_j = -1 + (j - 1/2)\Delta y \;\; j = 1 \cdots Y \quad \text{and } \Delta y = \frac{2}{Y} \\ z_k = -1 + (k - 1/2)\Delta z \;\; k = 1 \cdots Z \quad \text{and } \Delta z = \frac{2}{Z} \end{array} \tag{21}$$

Voxels on which the image intensity is constant are then defined as intervals $[U_i, U_{i+1}] \times [V_j, V_{j+1}] \times [W_k, W_{k+1}]$ with

$$\begin{array}{ll} U_i = x_i - \Delta_x/2 & U_{i+1} = x_i + \Delta_x/2 \\ V_j = y_j - \Delta_y/2 & V_{j+1} = y_j + \Delta_y/2 \\ W_k = z_k - \Delta_z/2 & W_{k+1} = z_k + \Delta_z/2 \end{array} \tag{22}$$

The moment expression computed on the whole image can then be rewritten as:

$$\begin{aligned} \lambda_{p,q,r} = C_{p,q,r} \sum_{i=1}^{L} \sum_{j=1}^{M} \sum_{k=1}^{N} \\ I(x_i, y_j, z_k) \int_{U_i}^{U_{i+1}} \int_{V_j}^{V_{j+1}} \int_{W_k}^{W_{k+1}} P_p(x) P_q(y) P_r(z) \mathrm{d}x \mathrm{d}y \mathrm{d}z \end{aligned} \tag{23}$$

Moreover thanks to the following recursive primitive property of the Legendre polynomials

$$\int_{cst}^{x} P_p(y)dy = \frac{P_{p+1}(x) - P_{p-1}(x)}{2p+1}, \tag{24}$$

Legendre moments can be written as:

$$\lambda_{pqr} = \sum_{i=1}^{L}\sum_{j=1}^{M}\sum_{k=1}^{N} I_p(x_i)I_q(y_j)I_r(z_k)I(x_i, y_j, z_k) \tag{25}$$

where $I_p(x_i) = \frac{2p+1}{2p+2}\left[xP_p(x) - P_{p-1}(x)\right]_{U_i}^{U_i+1}$ and similar expressions for I_q and I_r. The kernel $I_pI_qI_r$ is independent of the image intensity and can therefore be precomputed. Moreover the separability property allows us to compute the 3D moments using three 1D steps. To guarantee scale and translation invariance, Legendre moments must be reformulated in the following way:

$$\lambda_{pqr} = C_{pqr}\int_{[-1,1]^3} P_p(\frac{x-x_0}{\mathcal{A}})P_q(\frac{y-y0}{\mathcal{A}})P_r(\frac{z-z_0}{\mathcal{A}})I(x,y,z)dxdydz \tag{26}$$

where (x_0, y_0, z_0) are the coordinates of the center of inertia of I and $\mathcal{A}$ is the volume of the shape.

6.2 Discriminating volumes by a finite number of Legendre moments

Two similar shapes have the same set of Legendre moments and two different shapes have two different sets of Legendre moments. However, since we work with scale and translation invariant moments, the set $\{\lambda_{0,0,0}, \lambda_{0,0,1}, \lambda_{0,1,0}, \lambda_{1,0,0}\}$ is the same for each shape and should not be used for discriminating between shapes. In order to illustrate the discriminative power of the moments, we consider four classes of shapes: *class 1:* heart alone, *class 2:* heart and aorta together, *class 3:* heart and liver together, *class 4:* heart and liver and aorta together.

Norm 2 error To highlight differences between Legendre moments of the four classes of shapes, we compute the square ℓ_2 norm between two shapes as $||\lambda_{\text{shape}_1} - \lambda_{\text{shape}_2}||_2^2$ where λ_{shape_i} is a vector storing successive Legendre moments of a shape. Comparing the measures for a finite number of moments from a mask of a reference heart and objects for the other classes we obtain the results displayed in Table 2. The comparisons are made between classes of shapes that could be mixed up in a segmentation algorithm without shape constraint.

	mean		min		max	
order / ref vs	5	15	5	15	5	15
other hearts	0.17	1.21	0.13	1.09	0.26	1.52
heart and liver	0.56	2.40	0.52	2.26	0.58	2.56
heart and aorta	0.61	2.38	0.44	2.13	0.69	2.50
heart and aorta and liver	0.53	2.38	0.45	2.19	0.62	2.60

Table 2: ℓ_2 norm of the difference between sets of Legendre moments between a reference heart shape and 13 masks of other hearts, 4 masks of hearts and liver, 4 masks of hearts and aorta, 4 masks of hearts and aorta and liver.

(a) (b) (c) (d) (e)

Figure 13: Examples of mask of: (a) reference heart, (b-c) two other hearts, (d) heart and aorta, (e) heart and liver.

Errors at order 5 are inferior to those at order 15. This is due to the fact that small order moments represent low frequency shape information. The gap between moment differences between hearts and between hearts and other structures is more important for order 5 (factor 5) than for order 15 (factor 2). It is due to the fact that at order 5, the difference between shapes of different classes is sufficiently important to discriminate between them, and in the same class differences are too small to well discriminate between shapes in that class.
In the following experiment we compare moments at a maximum order 10 in order to well differentiate shapes and to take advantage of the global representation of a shape by its moments.

PCA analysis We now study the capability of Legendre moments to efficiently discriminate between correctly segmented hearts and erroneous segmentations, by considering again the four classes of shapes. Inspired by [37], we performed a PCA analysis on a matrix in which each raw is an observation, i.e. a segmentation result, and each column corresponds to an ordered list of Legendre moments. The PCA analysis revealed that the first three modes represent 90% of the variance. As illustrated in Figure 14, the moments also discriminate efficiently the different types of shapes. Indeed samples from the heart alone are well clustered in the plane of the first two modes and are well separated from the other types of shapes.

6.3 Introducing shape constraint in the segmentation functional

We propose to introduce an additional term in the segmentation functional to optimize a comparison between moments of a reference shape and moments of the current segmented shape, as follows:

$$\min_{u\in BV([0,1])} \left[\int_\Omega g|\nabla u| \mathrm{d}\Omega + \tau \int_\Omega r(\mathbf{x}) u \mathrm{d}\Omega + \frac{\gamma}{2} ||\lambda^{\mathrm{ref}} - \lambda^{\mathrm{cur}}(u)||_2^2 \right] \tag{27}$$

Where λ^{ref} is the vector of Legendre moments of the shape of reference and $\lambda^{\mathrm{cur}}(u)$ is the vector of Legendre moments of the segmentation.
This formulation is quite similar to the one described in [20]. However, using a membership function u instead of a level set function leads to a more stable algorithm. Another difference concerns the order of the used moments. Also one of the main objectives of the work in [20] was to provide an algorithm robust to occlusions, a hard constraint on the shape was needed and high order moments

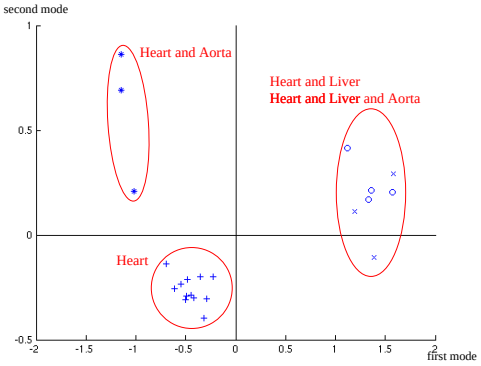

Figure 14: PCA on Legendre moments. Result on the first two principal axes, "+" heart alone, "o" heart and liver, "*" heart and aorta, "x" heart and liver and aorta.

were computed. In our framework, the goal is to capture global features of the shape but still allow a small variability between them. Therefore only small order moments are used.

Minimization We perform the minimization of the functional (27) by a gradient descent method. To insure that $u \in BV_{[0,1]}(\Omega)$ in (27) we rewrite the minimization problem in the same manner as in [38] :

$$\begin{aligned}\min_u E_{TV_g}(u(\mathbf{x})) = \min_u \Big[\int_\Omega g|\nabla u| \mathrm{d}\Omega + \tau \left(\int_\Omega u(\mathbf{x}) r(\mathbf{x}) \mathrm{d}\Omega \right) \\ + \int_\Omega \alpha \nu_\epsilon(u) \mathrm{d}\Omega + \frac{\gamma}{2} ||\lambda^{\mathrm{ref}} - \lambda^{\mathrm{cur}}(u)||_2^2 \Big]\end{aligned} \tag{28}$$

where ν_ϵ is a regularized approximation of the penality function $\nu(a) = \max\{0, 2|a-1/2|-1\}$ with $\alpha > ||r(\mathbf{x})+|| \, ||\lambda^{\mathrm{ref}} - \lambda^{\mathrm{cur}}(u)||_2^2||_\infty$ and we obtain the following iterative scheme:

$$\begin{aligned}u^{(n+1)}(\mathbf{x}) = u^n(\mathbf{x}) + dt \Big[\mathrm{div}(g \frac{\nabla u(\mathbf{x})}{|\nabla u(\mathbf{x})|}) - \tau r(\mathbf{x}) - \alpha \nu_\epsilon'(u) \\ - \gamma \sum_{p,q,r} \left((\lambda^{\mathrm{ref}}_{p,q,r} - \lambda^{\mathrm{cur}}_{p,q,r}(u)) P_p(x) P_q(y) P_r(z) \right) \Big]\end{aligned}$$

Design of the homogeneity term r Let us arbitrarily define the organ of interest region as the foreground region, (i.e. the region in which we would like to obtain $u(\mathbf{x}) = 1$) and the rest of the region of interest as the background region (i.e. the region in which we would like to obtain $u(\mathbf{x}) = 0$).
Taking as an example the segmentation of the heart, histograms of the foreground and the background intensities, obtained from manual segmentations, are shown in Figure 15. They show that intensity ranges of values are quite similar in the background and in the foreground. However, the histogram is very homogeneous in the heart while being more spread and presenting two peaks in the background.

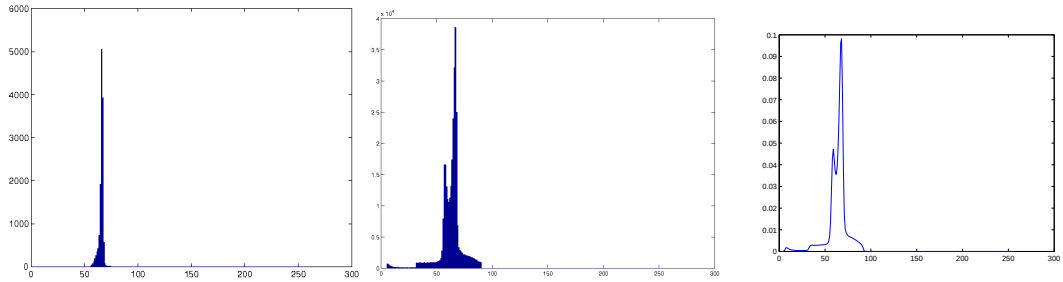

Figure 15: Histograms of foreground (left) and background (middle) intensities. Right: background intensity probability density estimation using Parzen window.

This leads us to construct the following data fidelity term $r(\mathbf{x})$:

$$r(\mathbf{x}) = (I - c_1)^2 - (\max((I(x) - c_1)^2))(\int_{\mathcal{B}} (p(b) - K(I - b))^2 db \tag{29}$$

where $c_1 = \frac{\int_\Omega I(\mathbf{x})u(\mathbf{x})d\mathbf{x}}{\int_\Omega u(\mathbf{x})d\mathbf{x}}$ is the empirical mean estimation of the organ intensity intensity, $\mathcal{B}$ is the interval of the voxels intensities, p is the Parzen estimation of the probability density function of the intensity of the background, expressed as:

$$p(b) = \frac{1}{||1 - u||_1} \int_\Omega (1 - u(\mathbf{x}))K((I(\mathbf{x}) - b)/\sigma)d\mathbf{x} \tag{30}$$

where the kernel K is a Gaussian window ($K(a) = \frac{1}{\sqrt{2\pi}} \exp(-\frac{a^2}{2})$) and σ is chosen sufficiently small to distinguish the two modes in the background area. This approach is similar to the one used in Section 3.

Choice of τ and γ As mentioned in Section 2, CT images are calibrated, with known tissue intensity values (for examples compact bones are known to be around 1000 HU). Such intensity calibration allows us to pre-set the weights of each term in the functional to insure good numerical balance between them. The regularization term, computed on manual segmentations, is of the order of 10^6 (corresponding to the surface area of whole heart weighted by the image based term $g = \frac{1}{1+|\nabla I|}$). The data fidelity term is close to zero. The shape constraint term (with fixed moment order to 10) falls within the range of values $[1, 2]$. Therefore, by dividing g by 10^6 a good balance between all terms in the functional (27) is obtained for τ and γ in the range $]0,\ 10[$. We performed several experiments for different parameters and finally we fixed $\tau = 1.4$ and $\gamma = 0.8$ for all tests summarized in Table 3.

6.4 Results for heart segmentation

Region of interest definition and initializing From a pre-segmentation of the lungs, a region of interest (ROI) around the heart is built as the bounding box of lungs elongated at the bottom to insure that the heart is completely included inside the ROI. A mask of the lungs and the trachea is easily removed from the ROI.

(a) (b) (c)

Figure 16: Heart segmentation setup. (a) Heart ROI definition with lungs and trachea masked out (in white) . (b) Example of an initialization of the hear region. (c) Gradient weighting function g enhancing contour around the heart.

	similarity index	sensitivity	specificity
Heart 1	0.82 (0.77)	0.96 (0.96)	0.74 (0.64)
Heart 2	0.81 (0.70)	0.89 (0.90)	0.78 (0.58)
Heart 3	0.80 (0.75)	0.94 (0.78)	0.70 (0.72)
Heart 4	0.84 (0.74)	0.76 (0.62)	0.97 (0.92)
Heart 5	0.77 (0.84)	0.81 (0.83)	0.72 (0.84)
Heart 6	0.81 (0.80)	0.93 (0.91)	0.71 (0.71)
Heart 7	0.78 (0.71)	0.84 (0.88)	0.73 (0.60)
Heart 8	0.80 (0.67)	0.92 (0.71)	0.80 (0.62)
Heart 9	0.75 (0.64)	0.83 (0.60)	0.73 (0.70)

Table 3: Quantitative results: comparison between automatic and manual segmentations. The numbers in parentheses are results obtained in [39].

Moreover tissues at the right of the left lung and at the left of the right lung are removed, as illustrated in Figure 16 (a).
The initialization of the heart's region is performed semi-automatically. A point C approximately at the center of the heart is manually marked and the initial value of $u(\mathbf{x})$ is defined as $u(\mathbf{x}) = 1$ if $\mathbf{x}$ is both inside a sphere centered at C with 4 cm diameter and inside the region of interest, and as $u(\mathbf{x}) = 0$ otherwise.

Tests and results Segmentations of the heart was evaluated on 9 non contrast CT scans. For each test, the result of the segmentation was compared with a manual delineation performed by an expert. Similarity, sensitivity and specificity indices are computed and reported in Table 3. We also compared our results with those obtained by the method of Moreno [39]. We globally obtain better results than those obtained by Moreno et al. Differences between the results of the two methods are illustrated in Figures 17(b) and 18. Except for the heart 4 (Figure 18 column 2), the specificity index is generally higher than the sensitivity. It means that our automatic segmentation often provides a larger region than the manual one (it is mainly due to the fact that a small part of the aorta is often included in the segmentation of the heart, as illustrated in Figure 17(a).

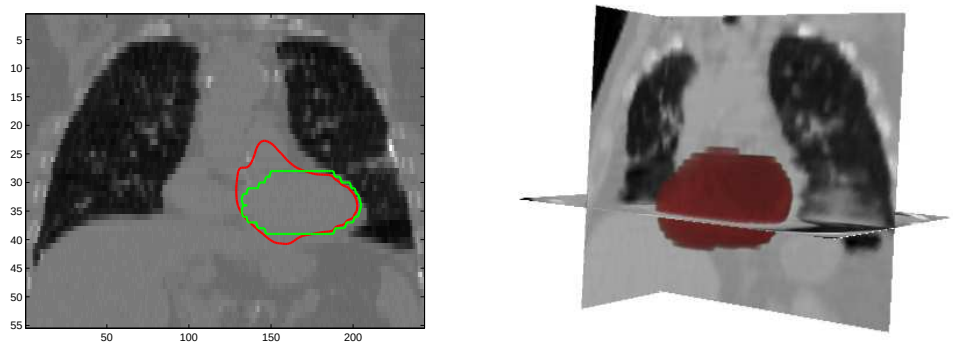

(a) (b)

Figure 17: (a) Automatic segmentation (in red) includes small part of the aorta (green: manual segmentation). (b) A 3D view of a whole heart segmentation.

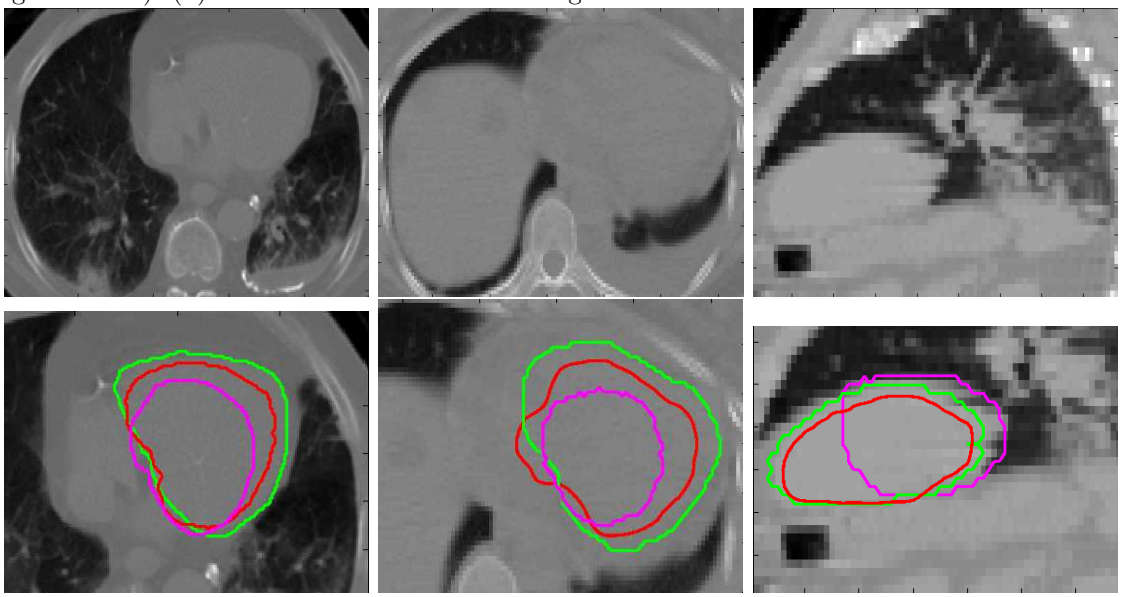

Figure 18: Examples of segmentation results. First row: original image, second row: image superimposed with segmentations (green expert segmentation, magenta Moreno et al segmentation, red our automatic segmentation).

7 Conclusion

We proposed a method to automatically segment thorax anatomical structures based on a hierarchical description. It allows us to use the strong knowledge about intensity distribution in a CT scan. Moreover, we proposed to incorporate a priori information to segment pathological structures such as lungs tumors and organs at risk for which a hierarchical description based only on grey

level distribution is not relevant.
Lungs tumors and infected lymph nodes are segmented using PET information and organs at risk are segmented using shape constraint. The quantitative evaluations show the interest of the proposed aproaches in both cases.

References

[1] Daisne, J.F.: Multi-Modality Imaging in Planning Patients with Head ans Neck Squamous Cell Carcinomas : Myths and Reality. PhD thesis, Université Catholique de Louvain (2005)

[2] Giraud, P., Elles, S., Helfre, S., Rycke, Y.D., Servois, V., Carette, M.F., Alzieu, C., Bondiau, P.Y., Dubray, B., Touboul, E., Housset, M., Rosenwald, J.C., Cosset, J.M.: Conformal radiotherapy for lung cancer: different delineation of the gross tumor volume (gtv) by radiologists and radiation oncologists. Radiotherapy and Oncology **62**(1) (2002) 27 – 36

[3] Erasmus, J.J., Gladish, G.W., Broemeling, L., Sabloff, B.S., Truong, M.T., Herbst, R.S., Munden, R.F.: Interobserver and intraobserver variability in measurement of non small cell carcinoma lung lesions: Implications for assessment of tumor response. Journal of Clinical Oncology **21**(4) (2003)

[4] Vinhais, C., Campilho, A.: Lung parenchyma segmentation from CT images based on material decomposition. In: ICIAR. (2006) II: 624–635

[5] Fasquel, J.B., Agnus, V., Moreau, J., Soler, L., Marescaux, J.: An interactive medical image segmentation system based on the optimal management of regions of interest using topological medical knowledge. Computer Methods and Programs in Biomedicine **82**(3) (2006) 216 – 230

[6] Camara, O., Colliot, O., Bloch, I.: Computational modeling of thoracic and abdominal anatomy using spatial relationships for image segmentation. Real-Time Imaging **10**(4) (August 2004) 263–273

[7] Naqa, I.E., Yang, D., Deasy, J.O.: Automated estimation of the biophysical target for radiotherapy treatment planning using multimodality image analysis. In: International Conference on Image Processing. (2007) V: 533–536

[8] Chan, T.F., Vese, L.A.: Active contours without edges. IEEE Trans. Image Processing **10**(2) (2001) 266–277

[9] Potesil, V., Huang, X., Zhou, X.: Automated tumor delineation using joint PET/CT information. In: Proc. of SPIE, Medical Imaging: Computer-aided Diagnosis. Volume 6514. (2007)

[10] Grubben, H., Miller, P., Hanna, G.G., Carson, K.J., Hounsell, A.R.: MAP-MRF segmentation of lung tumours in PET/CT image. In: International Symposium on Biomedical Imaging. (2010) 290–293

[11] Gastaud, M., Barlaud, M., Aubert, G.: Combining shape prior and statistical features for active contour segmentation. IEEE Trans. Circuits and Systems for Video Technology **14**(5) (May 2004) 726–734

[12] Leventon, M.E., Grimson, W.E.L., Faugeras, O.D.: Statistical shape influence in geodesic active contours. In: CVPR. (2000) I: 316–323

[13] Cootes, T.F., Taylor, C.J.: Statistical models of appearance for medical image analysis and computer vision. In: SPIE. (February 27 2001)

[14] Tsai, A., Yezzi, A.J., Willsky, A.S.: Curve evolution implementation of the mumford-shah functional for image segmentation, denoising, interpolation, and magnification. IEEE Trans. Image Processing **10**(8) (August 2001) 1169–1186

[15] Bresson, X., Vandergheynst, P., Thiran, J.P.: A priori information in image segmentation: energy functional based on shape statistical model and image information. In: ICIP. (2003) III: 425–428

[16] Yang, J., Duncan, J.S.: 3d image segmentation of deformable objects with joint shape-intensity prior models using level sets. Medical Image Analysis **8**(3) (2004) 285 – 294 Medical Image Computing and Computer-Assisted Intervention - MICCAI 2003.

[17] Bresson, X., Vandergheynst, P., Thiran, J.P.: A variational model for object segmentation using boundary information and shape prior driven by the mumford-shah functional. International Journal of Computer Vision **68**(2) (June 2006) 145–162

[18] Cremers, D., Rousson, M., Deriche, R.: A review of statistical approaches to level set segmentation: Integrating color, texture, motion and shape. International Journal of Computer Vision **72**(2) (April 2007) 195–215

[19] Rose, J.L., Revol-Muller, C., Charpigny, D., Odet, C.: Shape prior criterion based on Tchebichef moments in variational region growing. In: ICIP. (2009)

[20] Foulonneau, A., Charbonnier, P., Heitz, F.: Affine-invariant geometric shape priors for region-based active contours. IEEE Trans. Pattern Anal. Mach. Intell **28**(8) (2006) 1352–1357

[21] Lecellier, F., Besson, S.J., Fadili, J., Aubert, G., Revenu, M., Saloux, E.: Region-based active contour with noise and shape priors. In: ICIP. (2006) 1649–1652

[22] Jackson, S.A., Thomas, R.M.: Cross-Sectional Imaging Made Easy. Churchill Linvingstone (2004)

[23] Bresson, X., Esedoglu, S., Vandergheynst, P., Thiran, J.P., Osher, S.J.: Fast global minimization of the active contour/snake model. Journal of Mathematical Imaging and Vision **28**(2) (2007) 151–167

[24] Mory, B., Ardon, R.: Fuzzy region competition: A convex two-phase segmentation framework. In: Scale Space and Variational Methods in Computer Vision. (2007) 214–226

[25] Mory, B., Ardon, R., Thiran, J.P.: Variational segmentation using fuzzy region competition and local non-parametric probability density functions. In: International Conference on Computer Vision. (2007) 1–8

[26] Chan, T., Esedoglu, S., Nikolova, M.: Algorithms for finding global minimizers of image segmentation and denoising models. Technical report, UCLA CAM Resport 04-54 (2004)

[27] Chambolle, A.: An algorithm for total variation minimization and applications. Journal of Mathematical Imaging and Vision **20**(1-2) (2004) 89–97

[28] Paragios, N., Deriche, R.: Geodesic active contours for supervised texture segmentation. In: CVPR. (1999) II: 422–427

[29] Anquez, J., Angelini, E.D., Bloch, I.: Segmentation of fetal 3D ultrasound based on statistical prior and deformable model. In: ISBI, IEEE (2008) 17–20

[30] Ni, K.Y., Hong, B.W., Soatto, S., Chan, T.F.: Unsupervised multiphase segmentation: A recursive approach. Computer Vision and Image Understanding **113**(4) (April 2009) 502–510

[31] Venel, Y., Garhi, H., de Muret, A., Baulieu, J.L., Barillot, I., Prunier-Aesch, C.: Comparison of six methods of segmentation of tumor volume on the 18F-FDG PETscan with reference histological volume in nonsmall cell bronchopulmonary cancers. Médecine Nuclaire **32**(6) (2008) 339 – 353

[32] Black, Q.C., Grills, I.S., Kestin, L.L., Wong, C.O., Wong, J.W., Martinez, A.A., Yan, D.: Defining a radiotherapy target with positron emission tomography. International Journal of Radiation Oncology Biology Physics **60**(4) (2004) 1272 – 1282

[33] Nestle, U., Kremp, S., Schaefer-Schuler, A., Sebastian-Welsch, C., Hellwig, D., Rubes, C., Kirsch, C.M.: Comparison of different methods for delineation of 18F-FDG PET-positive tissue for target volume definition in radiotherapy of patients with non-small cell lung cancer. The Journal of nuclear medicine **46**(8) (2005) 1342 – 1348

[34] Heimann, T., van Ginneken etal, B.: Comparison and evaluation of methods for liver segmentation from CT datasets. IEEE Trans. Medical Imaging **28**(8) (August 2009) 1251–1265

[35] Teague, M.R.: Image analysis via the general theory of moments. Journal of the Optical Society of America **70**(8) (August 1980) 920–930

[36] Hosny, K.M.: Exact Legendre moment computation for gray level images. Pattern Recognition **40**(12) (December 2007) 3597–3605

[37] Poupon, F., Mangin, J.F., Hasboun, D., Poupon, C., Magnin, I.: Multi-object deformable templates dedicated to the segmentation of brain deep structures. In: Medical Image Computing and Computer-Assisted Intervention - MICCAI 1998. (1998)

[38] Chan, T.F., Esedoglu, S., Nikolova, M.: Finding the global minimum for binary image restoration. In: ICIP. (2005) I: 121–124

[39] Moreno, A., Takemura, C.M., Colliot, O., Camara, O., Bloch, I.: Using anatomical knowledge expressed as fuzzy constraints to segment the heart in CT images. Pattern Recognition **41**(8) (August 2008) 2525–2540

Dépôt légal : 2010 – 3ème trimestre
Imprimé à Télécom ParisTech – Paris
ISSN 0751-1345 ENST D (Paris) (France 1983-9999)

Télécom ParisTech

Institut TELECOM - membre de ParisTech

46, rue Barrault - 75634 Paris Cedex 13 - Tél. + 33 (0)1 45 81 77 77 - www.telecom-paristech.frfr

Département TSI